Science Bulletin 64 (2019) 595–602

Contents lists available at ScienceDirect

Science Bulletin

journal homepage: www.elsevier.com/locate/scib

Science Bulletin
www.scibull.com

Article

Highly sensitive ethanol gas sensor based on ultrathin nanosheets assembled Bi_2WO_6 with composite phase

Tongwei Yuan [a], Zhijun Li [c], Wenshuang Zhang [a], Zhenggang Xue [b], Xiaoqian Wang [b], Zhiheng Ma [a], Yu Fan [a], Jiaqiang Xu [a,*], Yuen Wu [b,*]

[a] New Energy and Sensing Technology Laboratory, Department of Chemistry, College of Science, Shanghai University, Shanghai 200444, China
[b] Department of Chemistry, iChEM (Collaborative Innovation Center of Chemistry for Energy Materials), University of Science and Technology of China, Hefei 230026, China
[c] Provincial Key Laboratory of Oil & Gas Chemical Technology, College of Chemistry and Chemical Engineering, Northeast Petroleum University, Daqing 163318, China

ARTICLE INFO

Article history:
Received 22 February 2019
Received in revised form 2 April 2019
Accepted 3 April 2019
Available online 5 April 2019

Keywords:
Bi_2WO_6
Nanosheets
Assembled structure
Composite phase
Gas sensor
Ethanol detection

ABSTRACT

Bismuth tungstate (Bi_2WO_6) has many intriguing properties and has been the focus of studies in a variety of fields, especially photocatalysis. However, its application in gas-sensing has been seldom reported. Here, we successfully synthesized assembled hierarchical Bi_2WO_6 which consists of ultrathin nanosheets with crystalline-amorphous composite phase by a one-step hydrothermal method. X-ray diffraction (XRD), X-ray photoemission spectroscopy (XPS), field-emission scanning electron microscopy (FESEM), and high-resolution transmission electron microscopy (HRTEM) techniques were employed to characterize its composition, morphology, and microstructure. By taking advantage of its unique microstructure, phase composition, and large surface area, we show that the resulting Bi_2WO_6 is capable of detecting ethanol gas with quick response (7 s) and recovery dynamic (14 s), extremely high sensitivity (R_a/R_g = 60.8@50 ppm ethanol) and selectivity. Additionally, it has excellent reproducibility and long-term stability (more than 50 d). The Bi_2WO_6 outperform the existing Bi_2WO_6-based and most of the other state-of-the-art sensing platforms. We not only provided one new member to the field of gas sensor, but also offered several strategies to reconstruct nanomaterials.

1. Introduction

Accurate and selective detection of volatile organic compounds (VOCs) is highly desirable for a variety of fields, for example, energy conservation, health and safety, and environmental pollution [1–4]. In recent years, different gas sensing materials such as semiconductor metal oxides, conducting polymers, organic functionalized carbon or silica, and fluorescent molecules have been synthesized, with significant improvements being made [5–8]. Amongst these, three-dimensional structure oxides with well-defined microstructures have been demonstrated to show excellent sensitivity and selectively, which can be attributed to their high surface area and hierarchy structures [9,10]. In addition, the typical three-dimensional structures provide an efficient gas diffusion channel to give fast gas response [11,12].

Ethanol is a common VOC and its efficient detection is important in several areas [13–15]. Many composite metal oxides have been reported to show good sensitivity to ethanol. For example, An et al. [16] synthesized Zn_2SnO_4 nanoparticles via a co-precipitation method and its gas-sensing performance to ethanol reached a value of R_a/R_g = 26.5@50 ppm (parts per million), where R_a is the sensor resistance in air, R_g is the sensor resistance in the test gas. Zhang group [17] fabricated Cl-doped nanocrystalline $LaFeO_{3-\delta}$ through a citric sol-gel method and obtained a superior ethanol gas sensing performance response of R_a/R_g = 79.2@200 - ppm. Lu and co-workers [18] prepared Al-NiO nanorod-flower by a solvothermal method and achieved a good response value of R_a/R_g = 12@100 ppm ethanol. Bismuth tungstate (Bi_2WO_6) is one of the Aurivillius composite oxide families of layered perovskites with corner-sharing WO_6 octahedral sheets and bismuth oxide sheets [19]. It has a variety of intriguing physical properties and a broad potential utility in photocatalysis, ferroelectric, and chemical sensors [20–22]. Despite its excellent semiconductor properties applied in the field of photocatalysis, few studies have examined the feasibility of employing Bi_2WO_6 in gas sensing [23,24]. Some strategies that improved the chemical reactivity of nanomaterial have been investigated by researchers, such as ultra-dispersed single-atoms [25–27], defect engineering [28] and reducing one dimension size of nanomaterial [29] and so on. Although some progress has been made, for example, synthesizing

* Corresponding authors.
E-mail addresses: xujiaqiang@shu.edu.cn (J. Xu), yuenwu@ustc.edu.cn (Y. Wu).

https://doi.org/10.1016/j.scib.2019.04.014
2095-9273/

Bi_2WO_6 with different morphologies, including nanoparticles, nanosheets, and nanospheres, the resulting improvement in ethanol gas sensing has been limited. This challenge drives us to develop a practical and facile approach to construct nanostructured Bi_2WO_6 to give further enhanced ethanol gas sensing performance.

In this work, we describe a facile hydrothermal approach with assistance of hexadecyl trimethyl ammonium chloride (CTAC) to synthesize a unique hierarchical multilayered Bi_2WO_6 architecture. Each layer exhibited an average thickness of 6.5 nm. Meanwhile, the crystalline-amorphous composite phase was formed because of the inhibitive function of CTAC in the process of crystal growth of Bi_2WO_6. A remarkable work has proved that the crystalline-amorphous composite phase has very outstanding chemical activity, comparing with traditional nanocrystal [30]. Then, this material was assembled into a gas sensor to validate its potential utility for ethanol gas sensing. The experimental results demonstrate its remarkable ethanol gas sensing performance (sensitivity, selectivity and stability). By contrast, without the assistance of CTAC, the Bi_2WO_6 is just large size aggregate with poor gas sensing properties, which has directly proved the validity of the strategies we have taken. Also, the gas sensing performances are superior to any of the existing Bi_2WO_6-based sensors.

2. Experimental

2.1. Chemicals and materials

Analytical grade sodium tungstate dihydrate ($Na_2WO_4{\cdot}2H_2O$), bismuth nitrate pentahydrate ($Bi(NO_3)_3{\cdot}5H_2O$), hexadecyl trimethyl ammonium chloride ($C_{16}H_{33}(CH_3)_3NCl$), and ethanol (CH_3-CH_2OH) were purchased from Shanghai Sinopharm Chemical Reagent Co., Ltd., China. Methane, hydrogen and carbon monoxide were purchased from Dalian Special Gases Co. Ltd. Analytical grade benzene, toluene, ammonia (25%), xylene, methanal (37%), acetone, and methanol were purchased from Shanghai Sinopharm Chemical Reagent Co., Ltd, China. Ultrapure water (18.2 MΩ) from Milli-Q System (Millipore, Billerica, MA) was used in experiments.

2.2. Preparation procedure

2.2.1. Synthesis of 3D nanoflower Bi_2WO_6 (NF-BWO)

After dissolving 120 mg of $Na_2WO_4{\cdot}2H_2O$ in 20 mL of deionized water, 60 mg CTAC was added and stirred for 5 min to give a uniform transparent solution. Then 295 mg $Bi(NO_3)_3{\cdot}5H_2O$ was added under stirring for 40 min to gain a milky suspension. Then it was transferred into a 25 mL Teflon-liner, sealed in a stainless autoclave, and placed in an oven at 150 °C for 20 h. After cooled down to room temperature, the as-product was centrifuged at 7,000 r/min for 5 min, washed with mixed solvent (50 vol% ethanol solution). After centrifugation and washing for five times, the sample was placed into vacuum drying oven at 70 °C for 12 h.

2.2.2. Synthesis of Bi_2WO_6

The process used to synthesis of Bi_2WO_6 was similar to NF-BWO but without addition of CTAC.

2.2.3. Synthesis of the product prepared by different addition sequence of reagents

A 295 mg powder of $Bi(NO_3)_3{\cdot}5H_2O$ was added into 20 mL of deionized water under stirring for 3 min. Then 60 mg of CTAC was dissolved into the suspension and 120 mg powder of $Na_2WO_4{\cdot}2H_2O$ was added and kept stirring for 40 min. The following steps were the same to the NF-BWO.

2.2.4. Synthesis of the samples prepared by different additive amount of CTAC

With the same operations to the NF-BWO except the amount of the addition of CTAC was changed to 30 and 90 mg.

2.3. Characterization

Powder X-ray diffraction patterns (PXRD) of samples were recorded at 0.02°/s on a Rigaku Miniflex-600 operating at 40 kV voltage and 15 mA current with Cu Kα radiation (λ = 0.15406 nm). The morphologies of the samples were observed by field emission scanning electron microscopy (FESEM, JSM-6700F), transmission electron microscope (TEM, JEM-200CX) and a high-resolution transmission electron microscope (HRTEM, JEM-2010, JEOL). To measure the thickness of NF-BWO, atomic force microscopy (AFM) image were captured by Dimension ICON with NanoScope V controller (Bruker) in ScanAsyst mode. Raman scattering spectra were recorded with a Renishaw System 2000 spectrometer using the 514.5 nm line of Ar+ for excitation. X-ray photoelectron spectroscopy (XPS) was collected on a thermofisher equipment (WSCALAB). Ultraviolet-visible diffuse reflectance spectroscopy (UV-DRS) was performed on Hitachi U-3010, using $BaSO_4$ as reference. Nitrogen sorption measurement was conducted using a Micromeritics ASAP 2020 system at 77 K.

2.4. Gas sensing measurements

2.4.1. Fabrication of gas sensors

NF-BWO or Bi_2WO_6 powder was mixed and ground with a small amount of ethanol to form a paste which subsequently was coated on an alumina ceramic tube with a fine brush, and then dried under an infrared lamp (about 0.1 mg sample for each tube). After transferred into a tubular furnace, it was heated to 250 °C for 2 h at a rate of 5 °C/min, and then cooled down to room temperature. This step was used to enhance the stability of the gas sensitive material. The four platinum wire pins of the core component were welded to the base of the gas sensor. And then Ni-Cr heating wire was inserted into the ceramic tube and welded. Install the base on the test circuit board. After aging at 250 °C for 5 d, the semiconductor components entered a stable performance period for gas sensing tests.

2.4.2. Measurement of gas sensing performance

The gas sensing tests were carried out on a WS-30A gas sensor measurement system (Hanwei Electronics Co. Ltd.). The test was carried out in a sealed container with a static valve chamber of 20 L. The liquid or gas was injected directly into the sealed space with a syringe. The characteristics of gas sensor were reported by measuring the output voltage (V_{out}) on the load resistance R_L connected in series with gas sensor. The work temperature was controlled by the heat voltage (V_{heat}), and the relationship between temperature and V_{heat} is shown as the Table S1 (online).

The testing conditions adopted in the measurement: the loop voltage was set at 5 V, adjusted V_{heat} from 2 to 5.5 V, the acquisition speed is 1 time/s, and the supply voltage is 220 V, 50 Hz. Define R_a is the resistance of sensor in the air and R_g is in the gas, then the calculation method is as follows.

$$\text{Response}: \ S = \frac{R_a}{R_g} \ (\text{reducing gas}), \tag{1}$$

$$\text{Response}: \ S = \frac{R_g}{R_a} \ (\text{oxidizing gas}). \tag{2}$$

3. Results and discussion

3.1. Synthesis and characterization

Our strategy to fabricate Bi_2WO_6 hierarchical architecture was mainly focused on the utilization of CTAC as an additive to fine tune the structure and the corresponding gas sensing properties (Fig. 1a). The synthetic route is shown in Fig. S1 (online). First, $Na_2WO_4{\cdot}2H_2O$, $Bi(NO_3)_3{\cdot}5H_2O$ and CTAC were mixed for hydrothermal reaction to give the white powder of nanoflower Bi_2WO_6 (NF-BWO). For comparison, a control sample (Bi_2WO_6) was prepared without addition of CTAC (Fig. S2 online) [31,32]. We also tested the influence of the sequence of addition of the reagents ($Na_2WO_4{\cdot}2H_2O$ and $Bi(NO_3)_3{\cdot}5H_2O$), as well as the usage of different amount of CTAC (0, 30, 60 and 90 mg). We found the use of 60 mg CTAC and order of $Bi(NO_3)_3{\cdot}5H_2O$ introduced into $Na_2WO_4{\cdot}2H_2O$ are critical to give the ideal product.

Surface morphologies of NF-BWO and Bi_2WO_6 were first explored by TEM, SEM and AFM. We observe the nanosheets of NF-BWO with a high purity was obtained, along with an average thickness of 6.5 nm (Fig. 1b). Furthermore, these ultrathin nanosheets were assembled into uniform three-dimensional hierarchical architecture (Fig. 1c).

However, the desired bismuth tungstate product cannot be synthesized by changing the order of addition of the reagents. Both product's morphologies tested by TEM and SEM (Fig. S3 online) are both quite anomalous. Because $Bi(NO_3)_3{\cdot}5H_2O$ has strong hydrolysis in pure water, it will produce a series of hydrolysis products, including $BiONO_3$, $Bi_2O_2(OH)NO_3$ and other intermediates. Some of these products may not participate in the formation of bismuth tungstate when sodium tungstate is subsequently added. By contrast, there are no impurities in the operation of adding sodium tungstate first. Because tungstate and bismuth ion could promote each other's hydrolysis and make the reaction proceed in the direction of producing bismuth tungstate. Moreover, we note that the addition of CTAC played an important role in the synthesis of NF-BWO. By changing the amount of CTAC from 0 to 90 mg but keeping the correct feeding sequence, different morphologies can be obtained (Fig. S4 online). Bi_2WO_6 agglomerate was produced without addition of CTAC. With the increase of CTAC from 0 to 60 mg, the assembled structure become more open and orderly. Therefore, the CTAC plays a critical role in the assembly process of nanomaterial. However, when excessive amount (90 mg) of the CTAC was used, the process of nucleation will be constrained. High-resolution TEM was carried out to provide further insights on the structural characteristics. We observe disordered areas are randomly distributed in crystalline phases of NF-BWO, giving numerous atoms at the crystalline-amorphous boundaries as shown in Fig. 1d. This is wholly different from the as-prepared Bi_2WO_6 which possess a single crystalline nature (Fig. S5 online). Generally, amorphous phases possess a higher surface activity in chemical reactions because of unsaturated surface atoms [33,34]. Moreover, the lattice spacing of 3.15 and 3.75 Å correspond to interplanar spacing of the (1 1 3) and (1 1 1) planes of orthorhombic NF-BWO.

The phase compositions of the samples were tested by X-ray powder diffraction (Fig. 2a). The diffraction peaks of NF-BWO and control sample can be indexed as orthorhombic Bi_2WO_6 (JCPDS No. 72-1126). In addition, the peaks of NF-BWO are relatively broader and lower in intensity compared to the control sample, suggesting a lower degree of crystallinity. This agrees well with the crystalline-amorphous composite phase observed by HRTEM. The XRD pattern of the sample produced by changing the sequence of addition of the reagents was also given (Fig. S6 online). We speculate it is likely attributed to hydrolysis of $Bi(NO_3)_3{\cdot}5H_2O$ in water. According to theoretical speculation and XRD data analysis, it is concluded that the impure crystalline phases mainly belong to $BiONO_3$ [35]. The resulting precipitates led to impurities in the product without ordered morphologies. The crystallinity of the sample decreases with the increase of CTAC (Fig. S7 online). Therefore, CTAC might be the key factor to introduce disordered areas on the surface of bismuth tungstate.

XPS was performed to determine the chemical composition of the samples. The XPS results show that the NF-BWO sample

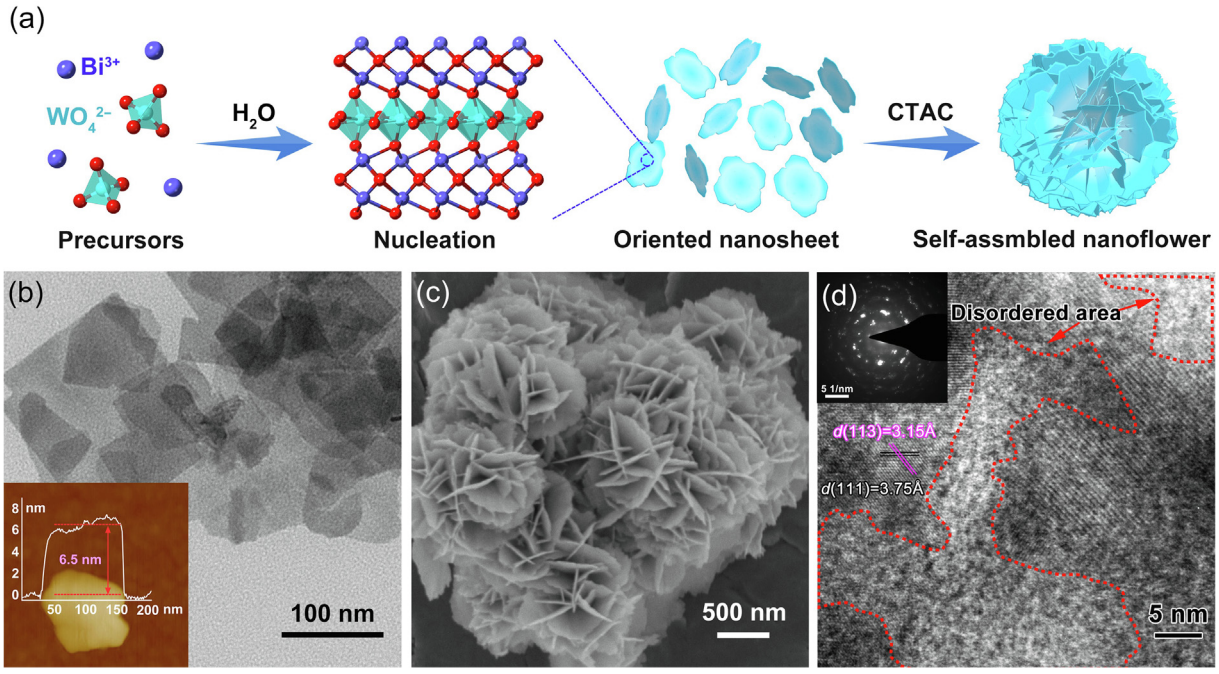

Fig. 1. (Color online) (a) Effect of CTAC on the assembly of the product. (b) TEM and AFM images of the corresponding nanosheets. (c) SEM image of the NF-BWO. (d) HRTEM image and the SAED of the NF-BWO nanosheet.

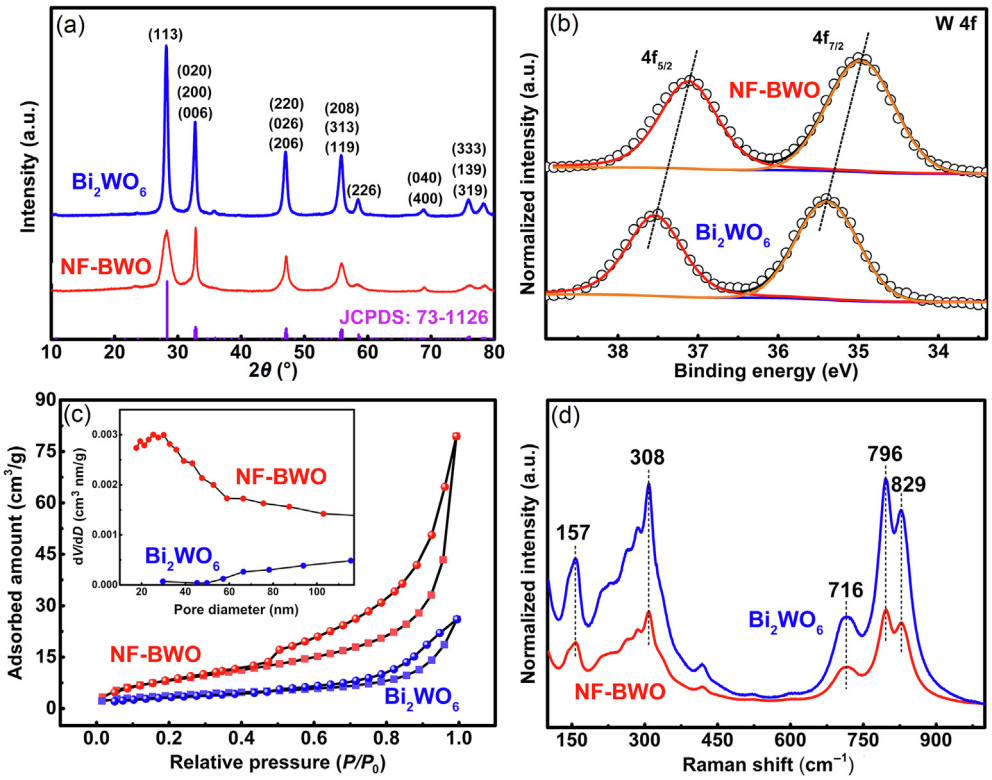

Fig. 2. (Color online) (a) XRD patterns of Bi_2WO_6 and NF-BWO. (b) XPS spectra of W 4f of Bi_2WO_6 and NF-BWO. (c) Nitrogen adsorption-desorption isotherms and Barrett-Joyner-Halenda (BJH) pore size distribution plot (insert graph) of Bi_2WO_6 and NF-BWO. (d) Raman spectra of Bi_2WO_6 and NF-BWO.

contains W, B, O, and a trace of C (Fig. S8 online). The C peak might result from contamination of the sample in the XPS chamber and can be used to calibrate other elements' peaks. For Bi, the two peaks observed at binding energies of 163.9 and 158.6 eV may be assigned to Bi $4f_{5/2}$ and Bi $4f_{7/2}$ respectively, and are consistent with the presence of a Bi^{3+} species in the sample. By comparing the W elements of both samples (Fig. 2b) peaked at 37.1 and 35.0 eV of NF-BWO and 37.5 and 35.4 eV of Bi_2WO_6, the peaks can be assigned to W $4f_{5/2}$ and W $4f_{7/2}$, respectively. This suggests a slight negative shift of W element in the surface of NF-BWO. The main difference between two samples' surfaces is that NF-BWO possesses crystalline-amorphous phase while Bi_2WO_6 is just crystalline. It could be attributed to the existence of disordered area because a part of W atoms might be unsaturated. This means that the valence of unsaturated W atoms maybe lower than the highest (VI) [36]. The O 1s spectrum of NF-BWO can be fitted to two peaks at 529.6 and 530.3 eV, corresponding to the crystal lattice in different chemical environments, being $[WO_4]^{2-}$ and $[Bi_2O_2]^{2+}$ layers (Fig. S9 online) [37]. For Bi_2WO_6, the corresponding peaks are at 529.1 and 531.1 eV. This means that a higher concentration of electrons caused by WO_4^{2-} is adsorbed onto the NF-BWO surface relative to Bi_2WO_6, giving rise to the negative shift binding energies.

The specific surface area was measured as it is an important factor that would affect the gas sensing performance [38,39]. The isotherms of two samples can be categorized as type IV with an H3 hysteresis loop, indicating the presence of mesopores (2–50 nm) (Fig. 2c). Type IV curve means the existence of mesopores while the H3 hysteresis loop indicates slit pores. Brunauer-Emmett-Teller (BET) surface areas tested for Bi_2WO_6 and NF-BWO are 13.50 and 31.12 m^2/g, respectively. Because slit pores are produced by the assembled structure, there are no penetrated pores existing in each nanosheet, which is highly consistent with the electron microscope photographs. Together, the NF-BWO has a higher specific surface area relative to Bi_2WO_6. This potentially provides a higher number of active sites and molecular transport channels, which would substantially improve the corresponding gas sensing properties [40].

The Raman spectra of NF-BWO and Bi_2WO_6 are shown in Fig. 2d. Specially the bands at 796 and 829 cm^{-1} can be ascribed to the antisymmetric and symmetric A_g modes of terminal O—W—O bonds. The band at 716 cm^{-1} is associated with an antisymmetric bridging associated with the tungstate chain. The band at 308 cm^{-1} can be ascribed to the translational modes of Bi^{3+} and WO_6^{6-} [41].

3.2. Evaluation of gas-sensing properties

We then assembled the sensing material NF-BWO into the gas sensor to evaluate its sensing performance to ethanol. The gas sensor consists of two gold electrodes, four Pt wires, an Al_2O_3 tube, a Ni-Cr heater, and a layer of gas-sensing materials (Figs. 3a and S10 (online)). The sensor and load resistor are connected in parallel to direct current circuit with voltage of 5 V (Fig. 3b) and then inject various gases into the gas sensing test machine. The electrical resistance of gas-sensing material, assembled in semiconducting metal oxides-based gas sensor, changes along with the effects of VOCs on the sensing materials [42]. The operating temperature was first optimized (Fig. 3c) as it directly affects the sensor's sensitivity to VOCs. The temperature could be adjusted by changing the heating voltage (Table S1 online) The results show the NF-BWO-based sensor reached its maximum response value of 60.8 to sensing 50 ppm ethanol at an operating temperature of 290 °C. By contrast, further increasing the operating temperature results in a decreased response trend. Therefore, 290 °C was employed as the optimal operating temperature in the present work. We further studied the selectivity of the sensing platform using 10 interfering

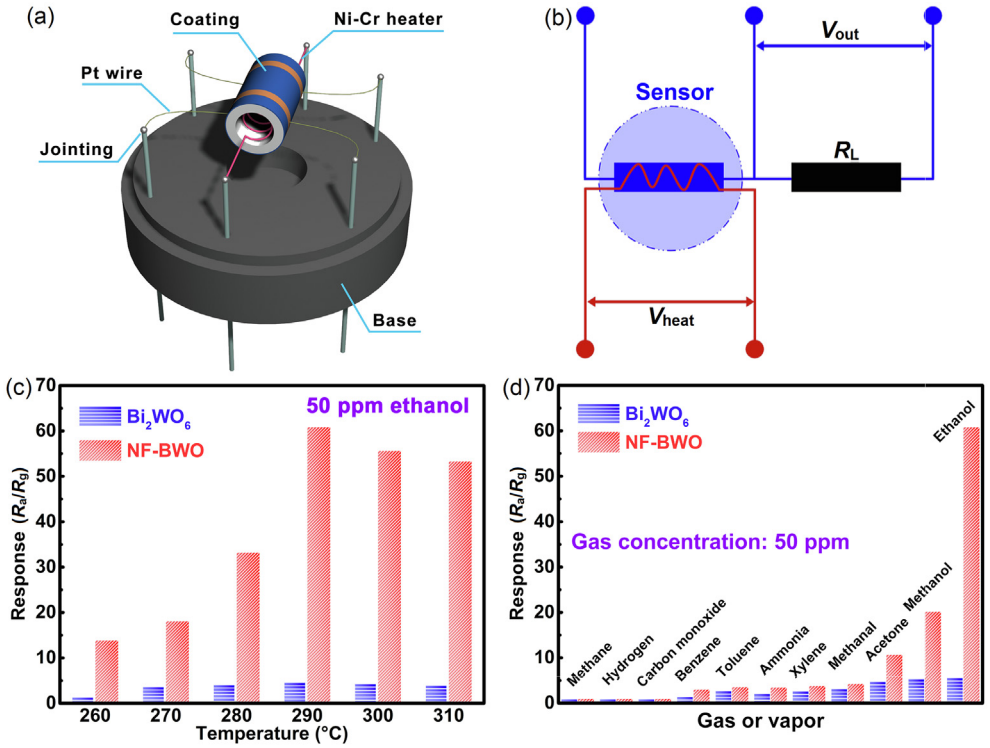

Fig. 3. (Color online) (a) Core sensing part of the sensor device. (b) The electric circuit structure of sensing part. (c) Operating temperature optimization of the sensors. (d) Selectivity of Bi_2WO_6 and NF-BWO.

gases at a concentration of 50 ppm (Fig. 3d). We notice the NF-BWO shows a highest response value to ethanol gas than other control gases, whereas the Bi_2WO_6 gives nearly indistinguishable responses to all gases. Specifically, the response value of NF-BWO to ethanol is approximately 10 times higher compared to that of Bi_2WO_6, suggesting excellent sensitivity and selectivity. Moreover, the response ratios of ethanol to other gases ($S_{ethanol}/S_{other\ gases}$) for NF-BWO and control sample are calculated and the values are in the ranges of 3.0–60.8 and 1.1–5.7, further demonstrating the excellent selectivity of our sensing material NF-BWO to ethanol gas (Table S2 online). Another important feature in the response signal is there are rapid response (7 s) and recovery (14 s) dynamics for NF-BWO in testing 50 ppm ethanol (Fig. 4a). For Bi_2WO_6 (Fig. S11 online) it shows a similar fast response and recovery (8 and 13 s). This is essential for assessing the performance of the sensing materials [43].

In order to establish a functional relationship between concentration and response value, we have tested the alcohol responses at different concentrations ranged from 1 to 50 ppm (Fig. 4b). The curve of voltage demonstrates a well-defined trend of response increase with the change of ethanol concentrations. The corresponding values of response exhibit a proportional relationship with ethanol vapor for concentrations from 5 ppm down to 1 ppm (Fig. 4c). Therefore, the linear equator is calculated as $y = 1.108 + 3.998\,x$ and the sum squared residual is 0.991. This means the NF-BWO-based sensor has an excellent linear relationship when the ethanol concentration is relatively low. Moreover, the data show that this platform can achieve an ultra-low limit of detection for ethanol gas down to 1 ppm ($R_a/R_g = 3.7$), as shown in Fig. S12 (online), superior to the corresponding values tested by Bi_2WO_6 (no obvious signal when exposed to 1 ppm ethanol) and most of the other sensing systems (Table S3 online). From Figs. 4c and S12 (online), a theoretical limit of detection of 0.11 ppm can also obtained ($S/N = 3$).

Reproducibility is a critically important factor for assessing the performance of the gas sensor. In our study, seven repeated cycles were tested on the gas sensor using 50 ppm ethanol gas and the result (Fig. 4d) shows essentially identical sensing performance (average ± standard deviation of the R_a/R_g tested: 60.5 ± 0.4). This reveals a superior reproducibility of the sensing platform. As for Bi_2WO_6 (Fig. S13 online), the response is also consistent, but the response is extremely low (average ± standard deviation of the R_a/R_g tested: 5.4 ± 0.3).

Long-term stability of the gas sensor is another key factor for validating this sensing platform. The sensing response of our gas sensor (NF-BWO) for 50 ppm ethanol was carried out for 50 d (Fig. 4e). The result shows the individual response was highly consistent throughout this period (average ± standard deviation of the R_a/R_g tested: 59.3 ± 2), demonstrating the exceptional long-term stability of the sensing material. Together, these data unambiguously validate the potential application of NF-BWO as an exceptional sensing material for ethanol gas sensing.

The performance data were measured under 40% RH humidity. To explore the effect of humidity on the response of gas sensitive materials, the humidity of test chamber was controlled from 25%−70% RH (Fig. 4f). It is found that the response of NF-BWO to 50 ppm ethanol is relatively stable under 50% RH humidity, along with a downward trend higher than 50% RH, because the adsorption of water affects the performance of gas sensitive materials.

3.3. Proposed sensing mechanism

The oxygen ionosorption can remove conduction electrons to give a lower conductance of semiconductors [44]. For NF-BWO and Bi_2WO_6-based sensors, the changes in resistance are predominantly by the adsorption and desorption of gas molecules on the sensing material surfaces. When the fabricated sensor is exposed to air, oxygen molecules can adsorb on the surface of sensing materials to form O_2^-, O^- and O^{2-} by capturing electrons from the conduction band (CB). This results in the formation of a thick space-charge layer that increase the potential carriers to give a higher resistance [45].

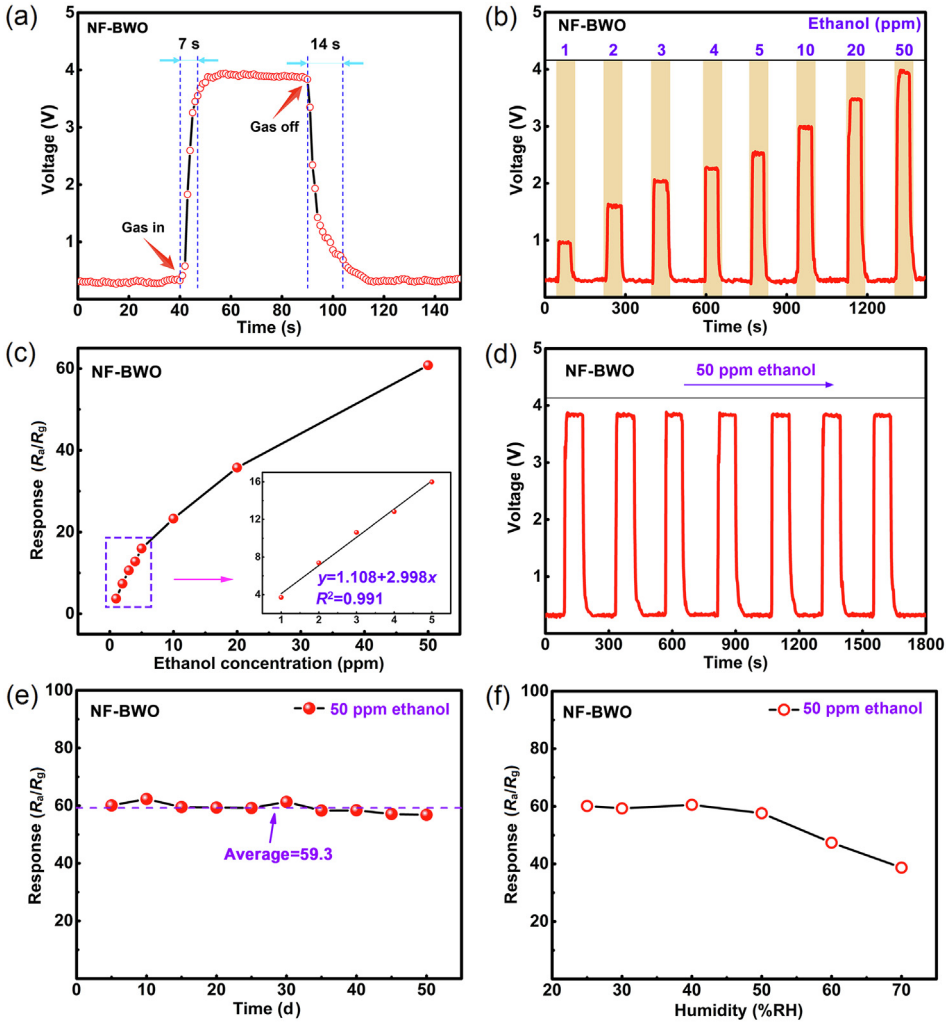

Fig. 4. (Color online) (a) Typical response signal of NF-BWO. Sensitivity (b) and the corresponding linear regression fitting (c) of NF-BWO for ethanol. Reproducibility (d) and long-term stability (e) of NF-BWO for 50 ppm ethanol. (f) Effect of humidity on the response of gas sensing material to 50 ppm ethanol.

$$O_{2(gas)} \rightarrow O_{2(ads)} \quad (1)$$

$$O_{2(ads)} + e^- \rightarrow O^-_{2(ads)} \quad (2)$$

$$O^-_{2(ads)} + e^- \rightarrow 2O^-_{(ads)} \quad (3)$$

The reactive oxygen species adsorbed on the surface of sensing materials are governed by temperature [46]. For example, O^{2-} is generally chemisorbed at low temperatures, whereas O^-_2 and O^- are chemisorbed at high temperatures. In our study, 290 °C was used as the operating temperature, therefore, the O^- species were predominantly contributed to the sensing behavior as follows:

$$CO_{(ads)} + O^-_{(ads)} \rightarrow CO_2 + e^- \quad (4)$$

$$H_{2(ads)} + O^-_{(ads)} \rightarrow H_2O + e^- \quad (5)$$

$$HCHO_{(ads)} + 2O^-_{(ads)} \rightarrow CO_2 + H_2O + 2e^- \quad (6)$$

$$C_2H_5OH_{(ads)} + 7O^-_{(ads)} \rightarrow 2CO_2 + 3H_2O + 7e^- \quad (7)$$

When reductive ethanol gas is introduced, it will react with adsorbed oxygen species on the sensing material to generate CO_2 and H_2O, and release electrons back to the conduction band of the sensing material, resulting in a reduced sensor resistance (Fig. 5) [47]. These equations indicate the electron donating effect of ethanol is stronger other gases. Meanwhile, comparing with BTEX (benzene, toluene, ethylbenzene and xylene) molecules, ethanol has a relative low reaction barrier [48].

Bi_2WO_6 is less sensitive in our experiments compared with NF-BWO. The facile strategy we have taken is adding an appropriate amount of CTAC to reshape the structure, resulting in the assembled hierarchical nanoflower which consists of ultrathin nanosheets with crystalline-amorphous phase. The reasons of gas sensing performance improvement of NF-BWO can be explained as follows. (1) Ultrathin nanosheet. When the oxygen molecules adsorb onto the surface of the semiconductor and then become oxygen ions by capturing the electrons from semiconductor. And the charge depletion layer has its depth. Therefore, if the thickness of semiconductor is small, the charge depletion layer would penetrate the whole nanosheet. This means the thin nanosheet has more electrons to expropriate than the thick one, resulting in more sensitive properties [49]. (2) Hierarchical assembly structure. The three-dimensional structure brings more specific surface area and gas diffusion channels, which are both significant to surface reactions. Also, each slit pore likes a micro-reactor that offer far more reaction sites than Bi_2WO_6 agglomerates [50]. (3) Crystalline-amorphous composite phase. The crystalline and amorphous phases are both significant, the unique structure of NF-BWO would not form without crystalline part while the amorphous part offer more active reaction sites [51].

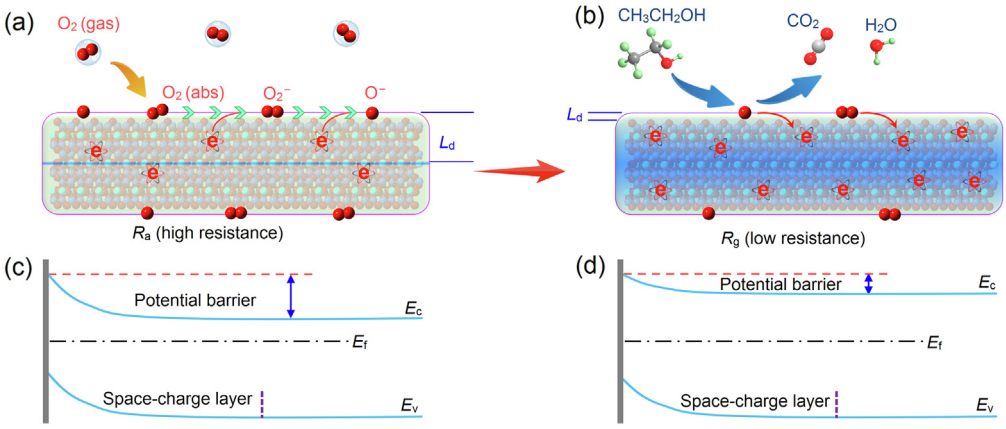

Fig. 5. (Color online) Proposed mechanism of NF-BWO-based gas sensor in air (a and c) and in ethanol (b and d).

Overall, the ultrathin nanosheet, unique three-dimensional structure and special crystalline-amorphous composite phase together contribute to the excellent sensing performance.

4. Conclusions

In summary, we have taken a facile strategy of introducing CTAC to reconstruct the structure of Bi_2WO_6, which successfully transfer a less sensitive material to remarkable ethanol gas sensing material. This method has been seldom reported previously. Specifically, this sensing material shows quick response and recovery dynamics, excellent sensitivity and selectivity, admirable reproducibility and exceptional long-term stability. Significantly, these performances of NF-BWO are generally far superior to the existing bismuth tungstate-based, implying the substantial promise of our NF-BWO-based sensor. Together, this study demonstrates the feasibility of employing NF-BWO in ethanol gas sensing, we have not only introduced a new member to the field of gas sensor, but also have offered an effective strategy to reform nanomaterials.

Conflict of interest

The authors declare that they have no conflict of interest.

Acknowledgments

This work was supported by the National Key R&D Program of China (2017YFA0208300 and 2017YFA0700104), the National Natural Science Foundation of China (61671284, U1704255, and 21671180). The authors acknowledge Prof. J. Hugh Horton (Queen's University) for a valuable discussion. The authors also acknowledge the support of the Shanghai Municipal Education Commission (Peak Discipline Construction Program).

Author contributions

Yuen Wu and Jiaqiang Xu designed the research; Tongwei Yuan performed the research; Wenshuang Zhang, Zhiheng Ma and Yu Fan participated in part of experiments; Zhijun Li, Xiaoqian Wang and Zhenggang Xue gave advices to article revision.

Appendix A. Supplementary data

Supplementary data to this article can be found online at https://doi.org/10.1016/j.scib.2019.04.014.

References

[1] Xue P, Yang X, Lai X, et al. Controlling synthesis and gas-sensing properties of ordered mesoporous In_2O_3-reduced graphene oxide (rGO) nanocomposite. Sci Bull 2015;60:1348–54.
[2] Broza YY, Vishinkin R, Barash O, et al. Synergy between nanomaterials and volatile organic compounds for non-invasive medical evaluation. Chem Soc Rev 2018;47:4781–859.
[3] Huang T, Lou Z, Chen S, et al. Fabrication of rigid and flexible $SrGe_4O_9$ nanotube-based sensors for room-temperature ammonia detection. Nano Res 2017;11:431–9.
[4] Shan H, Liu C, Liu L, et al. Excellent ethanol sensor based on multiwalled carbon nanotube-doped ZnO. Chin Sci Bull 2014;59:374–8.
[5] Zhu Y, Zhao Y, Ma J, et al. Mesoporous tungsten oxides with crystalline framework for highly sensitive and selective detection of foodborne pathogens. J Am Chem Soc 2017;139:10365–73.
[6] Wang L, Wang Z, Xiang Q, et al. High performance formaldehyde detection based on a novel copper(II) complex functionalized QCM gas sensor. Sens Actuat B 2017;248:820–8.
[7] Goud DR, Purohit AK, Tak V, et al. A highly selective and sensitive "turn-on" fluorescence chemodosimeter for the detection of mustard gas. Chem Commun 2014;50:12363–6.
[8] Zhou X, Lee S, Xu Z, et al. Recent progress on the development of chemosensors for gases. Chem Rev 2015;115:7944–8000.
[9] Govindhan M, Sidhureddy B, Chen A. High-temperature hydrogen gas sensor based on three-dimensional hierarchical-nanostructured nickel-cobalt oxide. ACS Appl Nano Mater 2018;1:6005–14.
[10] Yang Y, Tian C, Wang J, et al. Facile synthesis of novel 3D nanoflower-like Cu_xO/multilayer graphene composites for room temperature NO_x gas sensor application. Nanoscale 2014;6:7369–78.
[11] Firooz AA, Mahjoub AR, Khodadadi AA. Highly sensitive CO and ethanol nanoflower-like SnO_2 sensor among various morphologies obtained by using single and mixed ionic surfactant templates. Sens Actuat B 2009;141:89–96.
[12] Huang J, Wu Y, Gu C, et al. Large-scale synthesis of flowerlike ZnO nanostructure by a simple chemical solution route and its gas-sensing property. Sens Actuat B 2010;146:206–12.
[13] Xue Z, Cheng Z, Xu J, et al. Controllable evolution of dual defect Zn_i and V_O associate-rich ZnO nanodishes with (0001) exposed facet and its multiple sensitization effect for ethanol detection. ACS Appl Mater Interfaces 2017;9:41559–67.
[14] Anoshkin IV, Nasibulin AG, Mudimela PR, et al. Single-walled carbon nanotube networks for ethanol vapor sensing applications. Nano Res 2012;6:77–86.
[15] Yan S, Zan G, Wu Q. An ultrahigh-sensitivity and selective sensing material for ethanol: α-/γ-Fe_2O_3 mixed-phase mesoporous nanofibers. Nano Res 2015;8:3673–86.
[16] An D, Wang Q, Tong X, et al. Synthesis of Zn_2SnO_4 via a co-precipitation method and its gas-sensing property toward ethanol. Sens Actua B 2015;213:155–63.
[17] Cao E, Wang H, Wang X, et al. Enhanced ethanol sensing performance for chlorine doped nanocrystalline $LaFeO_{3-\delta}$ powders by citric sol-gel method. Sens Actuat B 2017;251:885–93.
[18] Wang C, Cui X, Liu J, et al. Design of superior ethanol gas sensor based on Al-doped NiO nanorod-flowers. ACS Sens 2015;1:131–6.
[19] Zhang N, Ciriminna R, Pagliaro M, et al. Nanochemistry-derived Bi_2WO_6 nanostructures: towards production of sustainable chemicals and fuels induced by visible light. Chem Soc Rev 2014;43:5276–87.
[20] Longo C, Galante TM, Fitzmorris R, et al. Complex oxides based on silver, bismuth, and tungsten: syntheses, characterization, and photoelectrochemical behavior. J Phys Chem C 2018;122:13473–80.
[21] Djani H, Hermet P, Ghosez P. First-principles characterization of the *P21ab* ferroelectric phase of Aurivillius Bi_2WO_6. J Phys Chem C 2014;118:13514–24.

[22] Lou Z, Deng J, Wang L, et al. Curling-like Bi_2WO_6 microdiscs with lamellar structure for enhanced gas-sensing properties. Sens Actuat B 2013;182:217–22.
[23] Li C, Chen G, Sun J, et al. Ultrathin nanoflakes constructed erythrocyte-like Bi_2WO_6 hierarchical architecture via anionic self-regulation strategy for improving photocatalytic activity and gas-sensing property. Appl Catal B Environ 2015;163:415–23.
[24] Wang D, Zhen Y, Xue G, et al. Synthesis of mesoporous Bi_2WO_6 architectures and their gas sensitivity to ethanol. J Mater Chem A 2013;1:4153.
[25] Wang X, Wang W, Qiao M, et al. Atomically dispersed Au_1 catalyst towards efficient electrochemical synthesis of ammonia. Sci Bull 2018;63:1246–53.
[26] Feng Q, Zhao S, He D, et al. Strain engineering to enhance the electrooxidation performance of atomic-layer Pt on intermetallic Pt_3Ga. J Am Chem Soc 2018;140:2773–6.
[27] Lu S, Zhuang Z. Investigating the influences of the adsorbed species on catalytic activity for hydrogen oxidation reaction in alkaline electrolyte. J Am Chem Soc 2017;139:5156–63.
[28] Li C, Yuan Q, Ni B, et al. Dendritic defect-rich palladium-copper-cobalt nanoalloys as robust multifunctional non-platinum electrocatalysts for fuel cells. Nat Commun 2018;9:3702.
[29] Ni B, Shi Y, Wang X. The sub-nanometer scale as a new focus in nanoscience. Adv Mater 2018;30:1802031.
[30] Cao X, Chen Z, Lin R, et al. A photochromic composite with enhanced carrier separation for the photocatalytic activation of benzylic C–H bonds in toluene. Nat Catal 2018;1:704–10.
[31] Zhang C, Zhu Y. Synthesis of square Bi_2WO_6 nanoplates as high-activity visible-light-driven photocatalysts. Chem Mater 2010;17:3537–45.
[32] Ma D, Huang S, Chen W, et al. Self-assembled three-dimensional hierarchical umbilicate Bi_2WO_6 microspheres from nanoplates: controlled synthesis, photocatalytic activities, and wettability. J Phys Chem C 2009;113:4369–74.
[33] Kuai L, Geng J, Chen C, et al. A reliable aerosol-spray-assisted approach to produce and optimize amorphous metal oxide catalysts for electrochemical water splitting. Angew Chem Int Ed 2014;53:7547–51.
[34] Yang N, Cheng H, Liu X, et al. Amorphous/crystalline hetero-phase Pd nanosheets: one-pot synthesis and highly selective hydrogenation reaction. Adv Mater 2018;30:1803234.
[35] Liu GQ, Zhong H, Li XR, et al. Research on nonenzymatic electrochemical sensor using HO-$BiONO_3$ nanocomposites for glucose detection. Sens Actuat B Chem 2017;242:484–91.
[36] Jia H, Stark J, Zhou LQ, et al. Different catalytic behavior of amorphous and crystalline cobalt tungstate for electrochemical water oxidation. RSC Adv 2012;2:10874.
[37] Huang H, Cao R, Yu S, et al. Single-unit-cell layer established Bi_2WO_6 3D hierarchical architectures: efficient adsorption, photocatalysis and dye-sensitized photoelectrochemical performance. Appl Catal B Environ 2017;219:526–37.
[38] Lu Y, Zhan W, He Y, et al. MOF-templated synthesis of porous Co_3O_4 concave nanocubes with high specific surface area and their gas sensing properties. ACS Appl Mater Interfaces 2014;6:4186–95.
[39] Koo WT, Yu S, Choi SJ, et al. Nanoscale PdO catalyst functionalized Co_3O_4 hollow nanocages using MOF templates for selective detection of acetone molecules in exhaled breath. ACS Appl Mater Interfaces 2017;9:8201–10.
[40] Wang H, Rogach AL. Hierarchical SnO_2 nanostructures: recent advances in design, synthesis, and applications. Chem Mater 2013;26:123–33.
[41] Shi R, Huang G, Lin J, et al. Photocatalytic activity enhancement for Bi_2WO_6 by fluorine substitution. J Phys Chem C 2009;113:19633–8.
[42] Lai X, Li J, Korgel BA, et al. General synthesis and gas-sensing properties of multiple-shell metal oxide hollow microspheres. Angew Chem Int Ed 2011;50:2738–41.
[43] Ma J, Ren Y, Zhou X, et al. Pt nanoparticles sensitized ordered mesoporous WO_3 semiconductor: gas sensing performance and mechanism study. Adv Funct Mater 2018;28:1705268.
[44] Lupan O, Ursaki VV, Chai G, et al. Selective hydrogen gas nanosensor using individual ZnO nanowire with fast response at room temperature. Sens Actuat B Chem 2010;144:56–66.
[45] Gao L, Ren F, Cheng Z, et al. Porous corundum-type In_2O_3 nanoflowers: controllable synthesis, enhanced ethanol-sensing properties and response mechanism. Cryst Eng Commun 2015;17:3268–76.
[46] Zhang J, Wang S, Wang Y, et al. Facile synthesis of highly ethanol-sensitive SnO_2 nanoparticles. Sens Actuat B Chem 2009;139:369–74.
[47] Zhou X, Zhu Y, Luo W, et al. Chelation-assisted soft-template synthesis of ordered mesoporous zinc oxides for low concentration gas sensing. J Mater Chem A 2016;4:15064–71.
[48] Zhang Y, Xu J, Xiang Q, et al. Brush-like hierarchical ZnO nanostructures: synthesis, photoluminescence and gas sensor properties. J Phys Chem C 2009;113:3430–5.
[49] Xu C, Tamaki J, Miura N, et al. Grain size effects on gas sensitivity of porous SnO_2-based elements. Sens Actuat B Chem 1991;3:147–55.
[50] Liu Y, Jiao Y, Zhang Z, et al. Hierarchical SnO_2 nanostructures made of intermingled ultrathin nanosheets for environmental remediation, smart gas sensor, and supercapacitor applications. ACS Appl Mater Interfaces 2014;6:2174–84.
[51] Kornienko N, Resasco J, Becknell N, et al. Operando spectroscopic analysis of an amorphous cobalt sulfide hydrogen evolution electrocatalyst. J Am Chem Soc 2015;137:7448–55.

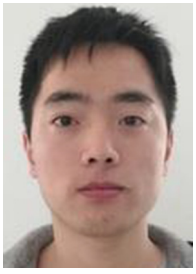

Tongwei Yuan is going to receive his M.S. degree in Shanghai University. He is currently making his efforts on functional nanomaterials, including zeolitic imidazolate frameworks, hydroxides, metal oxides and corresponding modification. His interests contain fabrication of gas sensor and synthesis of inorganic materials.

Jiaqiang Xu obtained his B.S. degree in Chemistry from Zhengzhou University, M.S. degree in Inorganic Chemistry from University of Science and Technology of China (USTC) and Ph.D. degree in Materials Science from Shanghai University, respectively. He has been a professor in Chemistry since 2001. His research interests include the synthesis of nanomaterials and their applications in gas sensors and other fields.

Yuen Wu received his B.Sc. and Ph.D. degrees from the Department of Chemistry, Tsinghua University in 2009 and 2014, respectively. He is currently a professor in the Department of Chemistry, University of Science and Technology of China. His research interests are focused on the synthesis, assembly, characterization and application of functional nanomaterials.